J. Fluid Mech. (2022), *vol*. 933, A26, doi:10.1017/jfm.2021.1077

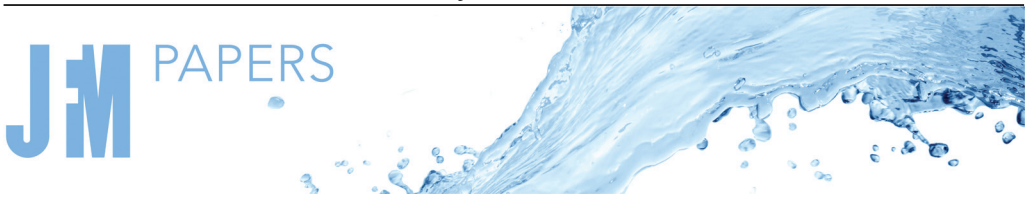

Instability of the attachment line boundary layer in a supersonic swept flow

Alexander V. Fedorov[1],† **and Ivan V. Egorov**[1,2]

[1]Moscow Institute of Physics and Technology (MIPT), 9 Institutsky per, Dolgoprudny, Moscow reg., 141701, Russia

[2]Central Aerohydrodynamic Institute (TsAGI), 1 Zhukovskogo Str, Zhukovsky, Moscow reg., 140180, Russia

(Received 22 June 2021; revised 24 November 2021; accepted 28 November 2021)

Theoretical analysis of attachment-line instabilities is performed for supersonic swept flows using the compressible Hiemenz approximation for the mean flow and the successive approximation procedures for disturbances. The theoretical model captures the dominant attachment-line modes in wide ranges of the sweep Mach number M_e and the wall temperature ratio. It is shown that these modes behave similar to the first and second Mack modes in the boundary layer flow. This similarity allows us to extrapolate the knowledge gained for Mack modes to the attachment-line instabilities. In particular, we find that at sufficiently large M_e, the dominant attachment-line instability is associated with the synchronisation of slow and fast modes of acoustic nature. Point-by-point comparisons of the theoretical predictions with the experiments of Gaillard *et al.* (*Exp. Fluids*, vol. 26, 1999, pp. 169–176) demonstrate that at $M_e > 4$, the theory captures a significant drop of the transition onset Reynolds number, which is below the contamination criterion of Poll ($R_* = 250$) at $M_e > 6$. This contradicts the generally accepted assumption that the attachment-line flow is stable for $R_* \leq 250$. The theoretical critical Reynolds numbers lie well below the experimental transition-onset Reynolds numbers. Stability computations using the Navier–Stokes mean flow and accounting for the leading-edge curvature effect do not eliminate this discrepancy. Most likely, in the experiments of Gaillard *et al*., we face with an unknown effect that does not fit to the concept of transition arising from linear instability.

Key words: high-speed flow, boundary layer stability, transition to turbulence

† Email address for correspondence: afedorov55@gmail.com

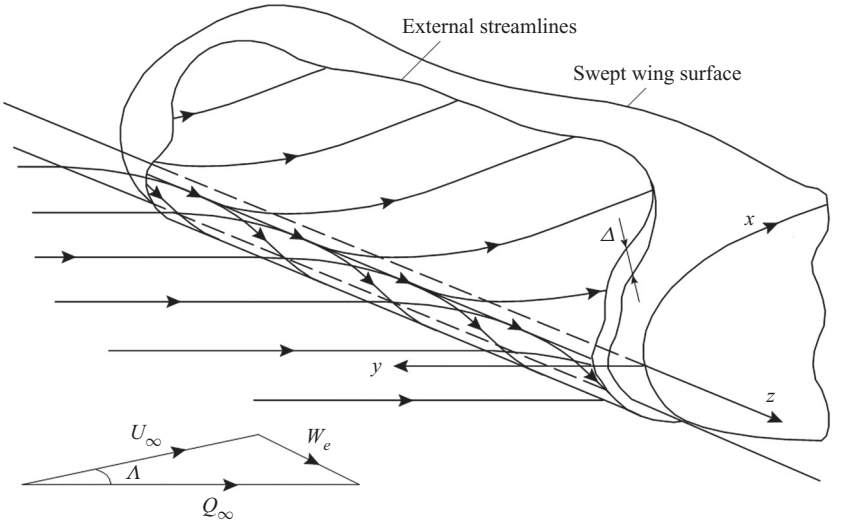

Figure 1. Flow scheme and notation.

1. Introduction

At supersonic speeds, the swept-wing leading edge is subject to high thermal loads. To facilitate the leading-edge thermal protection, it is required to predict and, if feasible, avoid the laminar–turbulent transition leading to a significant increase of aerodynamic heating.

If the swept leading edge is smooth and it is not contaminated by free-stream disturbances, transition follows the low-disturbance scenario including the three major stages (Morkovin, Reshotko & Herbert 1994): excitation of unstable modes of small initial amplitude (receptivity stage), spatial growth of instability along the attachment line (amplification stage governed by the linear stability theory) and nonlinear breakdown leading to a turbulent boundary-layer flow. Low-speed experiments (see Poll 1979) showed that this scenario is relevant to the case where transition is observed at the Reynolds number $R \equiv W_e^* \Delta^* / \nu_e^* \approx 650$. Hereafter, $\Delta^* = (\nu_e^* / \mathrm{d}U_e^*/\mathrm{d}x^*)^{1/2}_{x^*=0}$ is a characteristic length scale associated with the boundary-layer thickness, the upper asterisk denotes dimensional quantities, and the subscript 'e' denotes quantities at the upper boundary-layer edge. The flow scheme and notations are shown in figure 1. In the range $250 < R < 650$, transition is sensitive to the leading-edge roughness, free-stream disturbances and other external forcing, which trigger early nonlinear breakdown with partial or complete bypass of the linear amplification stage. For $R \leq 250$, the contaminated attachment-line flow is relaminarised: initial disturbances decay and the laminar flow sets in again.

Review of similar experiments at supersonic speeds is given by Lin & Malik (1995), see also Benard, Sidorenko & Raghunathan (2002). Analysing these data, Poll (1994) introduced the reduced Reynolds number $R_* \equiv W_e^* \Delta^*(\nu^*)/\nu^*$, where the kinematic viscosity ν^* is calculated at the reference temperature

$$T_*^* = T_e^* + 0.1(T_w^* - T_e^*) + 0.6(T_r^* - T_e^*), \tag{1.1}$$

where $T_r^* = T_e^*(1 + \sqrt{Pr}((\gamma - 1)/2)M_e^2)$ is the recovery temperature, $M_e = W_e^*/a_e^*$ is the local Mach number and the subscript 'w' denotes quantities on the wall surface.

However, the low disturbance environment criterion $R_{*tr} \approx 650$ poorly correlates with transition data obtained on smooth swept cylinders at large sweep Mach numbers.

Namely, in the wind-tunnel experiments of Gaillard, Benard & Alziary de Roquefort (1999) for $M_e > 4$, the transition onset Reynolds number decreases with M_e and for $M_e > 6$, approaches the contamination level $R_{*tr} = 250$.

Xi, Ren & Fu (2021) recently performed a numerical study of the attachment-line instability for the conditions relevant to the experiments of Gaillard *et al.* (1999). Using the Navier–Stokes (N-S) mean flow on a swept cylinder, they carried out stability analysis based on two-dimensional partial differential equations (2-D PDE). It was shown that, in the relatively low speed region ($M_e < 4$), the attachment-line modes can be treated as an extension of Tollmien–Schlichting (TS) modes (Lin & Malik 1995), while in the high speed region ($M_e > 4$), the attachment-line modes are closer to the Mack modes (Mack 1975) of the inviscid nature. The behaviour of the Mack-like modes explains why the critical transition Reynolds number decreases as the sweep Mach number increases in the experiment of Gaillard *et al.* (1999).

However, Xi *et al.* (2021) did not show detailed point-by-point comparisons with the transition data. It is not clear under what conditions the Mack-like modes compete with the TS-like modes and become dominant. Moreover, we found that the N-S mean flow solutions, which were used by Xi *et al.* (2021) in their stability analyses, do not agree with our N-S solutions and the compressible Hiemenz solution, which casts doubt on the correctness of the results reported.

To clarify this situation, we conduct a broadband parametric study, which is difficult to perform using the computationally expensive 2-D PDE approach of Xi *et al.* (2021). We put together and employed the following theoretical model: (1) the mean-flow parameters at the upper boundary-layer edge are calculated using the inviscid theory of Rechotko & Beckwith (1958); (2) the boundary-layer profiles are computed using the compressible Hiemenz solution (Pfenninger 1965, Gaster 1967); (3) the stability problem, which describes discrete modes propagating in the laminar attachment-line boundary layer, is solved using the theoretical model of Theofilis, Fedorov & Collis (2006), see also Semisynov *et al.* (2003). The model is based on successive approximation procedures of the type formulated independently by Gaster (1974) and Bouthier (1972, 1973).

This approach is based on the following findings. In the low-speed cases (incompressible flow), the Hiemenz solution agrees well with the mean flow measurements of Gaster (1967) and Poll (1979). The temporal stability of the incompressible Hiemenz flow was analysed by Hall, Malik & Poll (1984) with the assumption that the unstable mode (hereafter, HMP mode) is symmetric and its chordwise velocity is a linear function of the x-coordinate. Hall & Malik (1986) analysed weakly nonlinear effects associated with the HMP mode. They showed that, apart from a small interval near the (linear) critical Reynolds number, finite-amplitude solutions bifurcate subcritically from the upper branch of the neutral curve. Both the weakly nonlinear theory and the numerical calculations showed the existence of supercritical finite-amplitude (equilibrium) states near the lower branch, which explains why the observed flow exhibits a preference for the lower branch modes. The direct numerical simulation of Spalart (1988) gave support to the use of the HMP ansatz. Balakumar & Trivedi (1998) obtained 2-D nonlinear equilibrium solutions by solving the full Navier–Stokes equations as a nonlinear eigenvalue problem. The behaviour of these solutions is consistent with the weakly nonlinear theory. Their secondary instability was investigated using the Floquet theory. The results showed that these 2-D finite amplitude neutral solutions are unstable to three-dimensional (3-D) disturbances.

Lin & Malik (1996) solved the 2-D PDE eigenvalue problem and found symmetric (S_j) and antisymmetric (A_j) discrete modes of the type $f(x, y)\exp(\mathrm{i}\beta z - \mathrm{i}\omega t)$, where

$\omega(\beta) = \omega_r(\beta) + \mathrm{i}\omega_i(\beta)$ is complex eigenvalue and $j = 1,\ 2, \ldots$ Computations showed that the HMP mode corresponds to the symmetric mode S_1 having the highest growth rate ω_i.

Theofilis *et al.* (2003) found that eigenmodes of the 2-D-PDE stability problem have a polynomial structure versus x and the 2-D eigenvalue problem can be reduced to a system of one-dimensional (1-D) problems of the Orr–Sommerfeld class. Using the successive approximation procedure of Gaster (1974), they derived a compact semi-analytical relationship providing quick computations of the eigenvalues ω for modes S_j and A_j. Theofilis *et al.* (2006) demonstrated that a similar relationship is valid for compressible attachment-line flows, albeit restricted to certain ranges of Reynolds number owing to the error of the second-order asymptotic terms scaled as $O(M_e^2/R^2)$. Considering the stability of the compressible Hiemenz flows at $M_e = 0.5$ and 0.9, Gennaro *et al.* (2013) obtained perfect agreement between the temporal growth rates ω_i of mode S_1 predicted by solving the 2-D-PDE stability problem and using the 1-D theoretical analysis.

In addition to reconsidering the cases reported by Xi *et al.* (2021) and correcting their results, this paper suggests a theoretical model, which captures the attachment-line modes and allows us to determine regions of their dominance in the $M_e - T_f$ space. This model helps to perform quick parametric studies of the compressible attachment-line instability, shed light on the mechanisms of instability and extrapolate the knowledge gained on the supersonic boundary layer stability to the attachment-line flow.

The rest of this paper is organised as follows. In § 2, we discuss the methodology and compare the theoretical growth rates of the most unstable mode with those resulting from the 2-D-PDE stability computations of Li & Choudhari (2008) in the case of $M_e = 1.69$. In § 3, parametric stability computations are performed to identify regions where one or another unstable mode is dominant. It will be shown that at sufficiently high M_e and low wall-temperature ratio $T_f \equiv T_w^*/T_r^*$, the attachment-line flow can support discrete modes of acoustic nature. The most unstable among them is similar to the Mack second mode in the flat-plate boundary layer. In § 4, we analyse experimental data reported by Gaillard *et al.* (1999) with emphasis on high local Mach numbers ($M_e > 4$) associated with large angles of the leading-edge sweep. The results are summarised in § 5.

2. Methodology

2.1. *Mean flow*

Consider the near-wall compressible laminar flow on a swept cylinder of radius r^* and infinite length in the spanwise direction z (figure 1). In this case, the flow field does not depend on z. Gas is perfect with constant specific heat ratio γ and Prandtl number Pr. The dimensionless viscosity $\mu = \mu^*/\mu_e^*$ is approximated by the power law $\mu(T) = T^m$ or the Sutherland law $\mu = T^{3/2}(1 + S)/(T + S),\ S = 110.4K/T_e^*$.

In the attachment line vicinity, the near-wall flow can be described by the compressible Hiemenz solution (Theofilis *et al.* 2006). For small values of Δ^*/r^*, the cylinder-surface curvature can be neglected. Then, the coordinate system $(x, y, z) = (x^*, y^*, z^*)/\Delta^*$ is locally Cartesian. The velocity components (u^*, v^*, w^*), temperature T^* and pressure P^* are scaled using W_e^*, T_e^* and $\rho_e^* W_e^{*2}$, where the flow parameters at the upper boundary-layer edge are calculated using the analytical relations derived by Rechotko & Beckwith (1958).

In the attachment line vicinity,

$$(u, v, w) = (\varepsilon x U(y), \varepsilon V(y), W(y)), \quad T = T(y), \quad P = (\gamma M_e^2)^{-1} - \varepsilon^2 x^2/2, \quad (2.1a\text{–}c)$$

where $\varepsilon = R^{-1}$ is assumed to be small. The mean-flow profiles $U(y), V(y), W(y), T(y)$ are governed by the ordinary differential equation (ODE) system

$$\left.\begin{gathered}(U^2 + VU')/T = 1 + \mu' T' U' + \mu U'' \\ VW'/T = \mu' T' W' + \mu W'' \\ U - VT'/T + V' = 0 \\ (\mu' T'^2 + \mu T'')/Pr - T'V/T + M_e^2(\gamma - 1)\mu W'^2 = 0\end{gathered}\right\}, \tag{2.2}$$

with the boundary conditions

$$\left.\begin{gathered}y = 0: \ U = V = W = 0 \\ T = T_w \text{ for isothermal wall, or } T' = 0 \text{ for thermally isolated wall} \\ y = \infty: \ U = W = T = 1\end{gathered}\right\}. \tag{2.3}$$

Note that for incompressible flows, the Hiemenz solution is an exact Navier–Stokes solution. For compressible flows, this is not the case owing to the error of the order of $O(\varepsilon^2 M_e^2)$. The system (2.2) is integrated numerically using the fourth-order Runge–Kutta algorithm. More than 400 grid points equally spaced versus y are needed to compute the boundary-layer profiles with six significant digits.

In addition, the laminar flow past a swept cylinder is calculated using the in-house N-S solver. The 2-D computational domain is limited by: the detached bow shock with the Rankine–Hugoniot conditions; the body surface with no-slip and isothermal boundary conditions; the symmetry line; and the chordwise edge, which corresponds to the azimuthal angle $\pi/2$, with the soft boundary condition – the linear extrapolation of dependant variables.

The problem is solved numerically using the method of bow-shock isolation (Egorov 1992). For approximation of convective and diffusion components of the flow vector in semi-integer nodes on the elementary cell edges, the second-order central difference scheme on a nine-point "box" stencil is used. This scheme does not belong to the family of monotone difference schemes and, therefore, cannot be used for solving problems with discontinuities. However, in the case where dependant variables are smooth and the physical dissipation is present, central difference schemes allow us to obtain more accurate solutions compared with monotone schemes on the same computational grids. To solve the nonlinear difference equations approximating the differential equations, the modified Newton–Raphson method is used. The system of linear algebraic equations obtained at each iteration step, is solved using the direct method of LU-decomposition with preliminary renumbering of unknowns by the nested dissection method.

Computations are performed on a non-uniform computational grid containing 201 nodes along the cylinder surface and 301 nodes in the wall normal direction. Near the shock wave and the body surface there are thin layers, which contain, after clustering, approximately 10 % and 55 % of the total number of nodes, respectively.

Figure 2 compares the theoretical and N-S mean-flow solutions for the case C3373a specified in table 2 of Appendix A. The profiles $U(y), W(y), T(y)$ and their derivatives agree very well. The discrepancy in $V(y)$ is not appreciable, because the vertical velocity $\varepsilon V(y)$ is not involved into the leading-order approximation of the eigenvalue problem for disturbances (see § 2.2).

This result disagrees with similar comparisons reported by Xi *et al.* (2021). Namely, the N-S mean-flow profiles differ significantly from the boundary layer approximation.

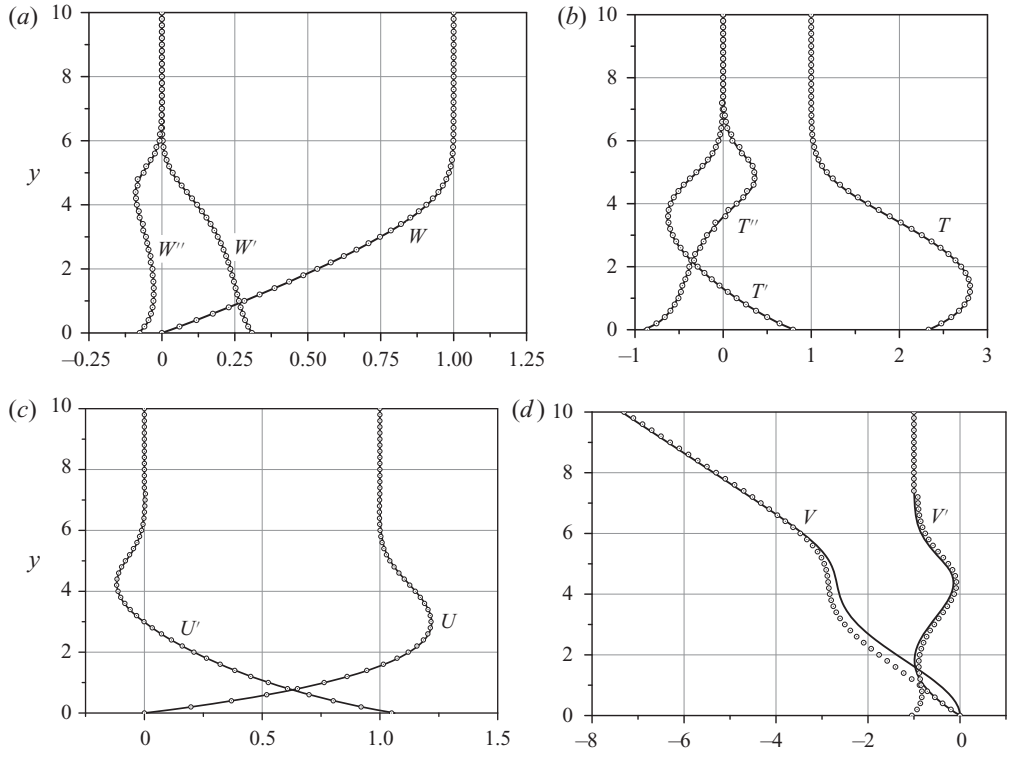

Figure 2. The mean flow profiles in case C3373a: lines, compressible Hiemenz solution; symbols, our N-S solution.

As shown in Appendix B, the N-S mean-flow solutions of Xi *et al.* (2021) are not correct. This led to the wrong conclusion: "the traditional boundary layer model fails to take the influence of inviscid flow into consideration this influence sometimes may change the physics of flow instability significantly..."

2.2. *Stability analysis*

The disturbance vector is expressed as

$$\boldsymbol{q}(x, y, z, t) \equiv \left(u, \frac{\partial u}{\partial y}, v, p, \theta, \frac{\partial \theta}{\partial y}, w, \frac{\partial w}{\partial y}\right)^T = \boldsymbol{F}(x, y)\exp[\mathrm{i}(\beta z - \omega t)], \tag{2.4}$$

where $t = t^* W_e^* / \Delta^*$ is time and θ is non-dimensional temperature. Because the attachment-line flow is convectively unstable, we consider the spatial stability problem, where ω is real and β is a complex eigenvalue with $\sigma = -\beta_i$ representing the growth rate of a wave propagating along the attachment line.

For quasi-2-D disturbances, the vector-function $\boldsymbol{F}$ is expanded as (Theofilis *et al.* 2006)

$$\boldsymbol{F} = \boldsymbol{Z}_0(y; x_1, z_1) + \varepsilon \boldsymbol{Z}_1(y; x_1, z_1) + \cdots, \tag{2.5}$$

where $x_1 = \varepsilon x$ and $z_1 = \varepsilon z$ are slow variables. In accord with the Gaster (1974) approach (see also Nayfeh 1980) the zero-order term is expressed as $\boldsymbol{Z}_0 = C(x_1, z_1)\boldsymbol{\xi}(y, x_1)$, where

$\boldsymbol{\xi}$ is solution of the problem

$$\left.\begin{aligned} \frac{\partial \boldsymbol{\xi}}{\partial y} &= \boldsymbol{A}\boldsymbol{\xi} \\ \xi_1 = \xi_3 = \xi_5 = \xi_7 &= 0, \quad y = 0 \\ \xi_1 = \xi_3 = \xi_5 = \xi_7 &= 0, \quad y = \infty \end{aligned}\right\}, \tag{2.6}$$

which delivers the eigenvalue $\beta = \beta_0(\omega, R)$. Here $\boldsymbol{A}$ is an 8×8 matrix of the linear stability problem. Its explicit form can be found in Mack (1979), Nayfeh (1980), Tumin (2007) and other papers. Note that some elements of this matrix include ε and therefore (2.5) is not a self-consistent asymptotic expansion. Nevertheless, Tumin (2006) showed that this inconsistency does not lead to an erroneous asymptotic behaviour of Tollmien–Schlichting waves. Numerous papers demonstrated robustness of this approach to receptivity and stability problems for weakly non-parallel compressible boundary-layer flows (for example, see the survey of Tumin 2011).

For the compressible Hiemenz flow, β_0 does not depend on x_1 while the eigenvector $\boldsymbol{\xi}$ can be expressed in the form

$$\boldsymbol{\xi}(x_1, y) = (x_1\xi_{01}(y), x_1\xi_{02}(y), \xi_{03}(y), \xi_{04}(y), \xi_{05}(y), \xi_{06}(y), \xi_{07}(y), \xi_{08}(y))^T. \tag{2.7}$$

In the first-order approximation, we obtain the inhomogeneous problem

$$\left.\begin{aligned} \frac{\partial \boldsymbol{Z}_1}{\partial y} &= \boldsymbol{A}\boldsymbol{Z}_1 + \boldsymbol{G}_x\frac{\partial \boldsymbol{Z}_0}{\partial x_1} + \boldsymbol{G}_z\frac{\partial \boldsymbol{Z}_0}{\partial z_1} + \boldsymbol{H}\boldsymbol{Z}_0 \\ Z_{11} = Z_{13} = Z_{15} = Z_{17} &= 0, \quad y = 0 \\ Z_{11} = Z_{13} = Z_{15} = Z_{17} &= 0, \quad y = \infty \end{aligned}\right\}, \tag{2.8}$$

where $\boldsymbol{G}_z = -\mathrm{i}\partial\boldsymbol{A}/\partial\beta$, $\boldsymbol{G}_x = -\mathrm{i}\partial\boldsymbol{A}/\partial\alpha$ and the matrix $\boldsymbol{H}$ depends on the mean-flow profiles $U(y)$ and $V(y)$.

The problem (2.8) has a non-trivial solution if the inhomogeneous part is orthogonal to the solution $\boldsymbol{\zeta}$ of the adjoint problem. This leads to the equation for the amplitude function $C(x_1, z_1)$

$$\langle \boldsymbol{G}_x\boldsymbol{\xi}, \boldsymbol{\zeta}\rangle\frac{\partial C}{\partial x_1} + \langle \boldsymbol{G}_z\boldsymbol{\xi}, \boldsymbol{\zeta}\rangle\frac{\partial C}{\partial z_1} + C\left[\left\langle \boldsymbol{G}_x\frac{\partial \boldsymbol{\xi}}{\partial x_1}, \boldsymbol{\zeta}\right\rangle + \langle \boldsymbol{H}\boldsymbol{\xi}, \boldsymbol{\zeta}\rangle\right] = 0, \tag{2.9}$$

where the scalar product is defined as $\langle \boldsymbol{\xi}, \boldsymbol{\zeta}\rangle = \int_0^\infty (\sum_{j,k=1}^{8} \xi_k\zeta_j)\,\mathrm{d}y$. Equation (2.9) can be written in a form similar to the incompressible case (Theofilis *et al.* 2003)

$$D_1 x_1\frac{\partial C}{\partial x_1} + D_2\frac{\partial C}{\partial z_1} + CD_3 = 0, \tag{2.10}$$

where $D_{1,2,3}$ are constants. Equation (2.10) admits the family of solutions

$$C_n = Bx_1^n\exp(\mathrm{i}\beta_{1n}z_1), \quad \beta_{1n} = i(D_3 + nD_1)/D_2, \tag{2.11}$$

where $n = 0, 1, 2, \ldots$ and B is constant.

Thus, quasi-2-D modes can be expressed as

$$\left.\begin{aligned} \boldsymbol{q}_n(x, y, z, t) &= Bx_1^n\boldsymbol{\xi}(x_1, y)[1 + O(\varepsilon)]\exp[i(\beta_n z - \omega t)] \\ \beta_n &= \beta_0 + \varepsilon\beta_{1n} + O(\varepsilon^2) \end{aligned}\right\}. \tag{2.12}$$

Here $n = 0, 2, \ldots$ correspond to symmetric modes S_1, S_2,... and $n = 1, 3, \ldots$ to antisymmetric modes A_1, A_2, ... These modes are calculated using the following

algorithm: (1) solve the zero-order problem (2.6) at $x_1 = 0$, which is a standard stability problem for 2-D waves in a 2-D boundary layer with the mean-flow profiles $W(y)$ and $T(y)$; (2) solve the corresponding adjoint problem; (3) calculate the eigenvalues β_n and the vector-functions $\boldsymbol{q}_n$ using (2.11) and (2.12).

For 3-D disturbances of the type

$$\boldsymbol{F} = [\boldsymbol{Z}_0(y; x_1, z_1) + \varepsilon \boldsymbol{Z}_1(y; x_1, z_1) + \cdots]\exp(\mathrm{i}\alpha x), \tag{2.13}$$

the zeroth-order vector function is expressed as $\boldsymbol{Z}_0 = C(z_1)\boldsymbol{\xi}(x_1, y)$, where $\boldsymbol{\xi}$ is a solution of the eigenvalue problem (2.6) with the complex eigenvalue $\beta = \beta_0(\omega, \alpha)$. In the first-order approximation, $\boldsymbol{Z}_1$ is a solution of the problem (2.8), while the amplitude coefficient is governed by the equation

$$\langle \boldsymbol{G}_z\boldsymbol{\xi}, \boldsymbol{\zeta}\rangle \frac{\partial C}{\partial z_1} + C\left[\left\langle \boldsymbol{G}_x \frac{\partial \boldsymbol{\xi}}{\partial x_1}, \boldsymbol{\zeta}\right\rangle + \langle \boldsymbol{H}\boldsymbol{\xi}, \boldsymbol{\zeta}\rangle\right] = 0. \tag{2.14}$$

Its solution is

$$C = B\exp(\mathrm{i}\beta_1 z_1), \quad \beta_1 = i\left[\left\langle \boldsymbol{G}_x \frac{\partial \boldsymbol{\xi}}{\partial x_1}, \boldsymbol{\zeta}\right\rangle + \langle \boldsymbol{H}\boldsymbol{\xi}, \boldsymbol{\zeta}\rangle\right] / \langle \boldsymbol{G}_z\boldsymbol{\xi}, \boldsymbol{\zeta}\rangle. \tag{2.15}$$

In summary, the 3-D mode is expressed as

$$\left.\begin{aligned} \boldsymbol{q}(x, y, z, t) = B\boldsymbol{\xi}(x_1, y)[1 + O(\varepsilon)]\exp[\mathrm{i}(\alpha x + \beta z - \omega t)] \\ \beta = \beta_0 + \varepsilon\beta_1 + O(\varepsilon^2) \end{aligned}\right\}, \tag{2.16}$$

Computations of quasi-2-D modes (2.12) and 3-D mode (2.16) are performed using an in-house linear stability solver. The fundamental solutions of the direct and adjoint eigenvalue problems are obtained by numerical integration of the equations from the upper boundary toward the wall with the known analytical asymptotic solutions outside the boundary layer using the Gramm–Schmidt orthonormalisation procedure and the fourth-order Runge–Kutta algorithm. Eigenfunctions of the direct and adjoint problems are expressed as a linear combination of the fundamental solutions, with coefficients being determined from the boundary conditions on the wall. To satisfy these conditions, the eigenvalues β are determined using the Newton–Raphson iterations.

The asymptotic solution (2.12) is validated by comparison with solutions of the 2-D-PDE stability problem reported by Li & Choudhari (2008) for the compressible Hiemenz flow at $M_e = 1.69$, $T_e^* = 300$ K, $T_w = T_{ad}$ (thermally isolated wall). Figure 3 shows that the theoretical growth rates $\sigma = -\beta_i(\omega)$ agree well with those predicted by the 2-D-PDE stability analysis for the first symmetric mode S_1. Similar comparisons for subsonic attachment-line flows ($M_e = 0.5$ and 0.9) were reported by Gennaro *et al.* (2013).

Because the compressible Hiemenz mean-flow profiles agree well with the corresponding N-S profiles (figure 2), it is expected that stability characteristics of these flows also agree well. This is confirmed by figure 4 showing the maximal growth rates $\sigma_{max}(R) = \max_\omega[-\beta_i(\omega, R)]$ of mode S_1 predicted by the theory in the case C3373a. A slight downward shift of σ_{max} in the case of N-S mean flow seems to arise from the curvature effect.

For small $\alpha : \alpha = a\varepsilon,\ a = O(1)$, the factor $\exp(\mathrm{i}\alpha x)$ in (2.16) can be expanded in the Taylor series: $\exp(\mathrm{i}\alpha x) = \sum_{n=0}^{\infty} (\mathrm{i}a)^n x_1^n/n!$, where $0! = 1$. Then the solution can be treated as a sum of symmetric ($n = 0, 2, \ldots$) and antisymmetric ($n = 1, 3, \ldots$) modes of the form (2.12). The dominant term of this expansion corresponds to $n = 0$. Consequently, in the attachment-line vicinity $x_1 \ll 1$, the 3-D mode of (2.16) tends to the symmetric quasi-2-D

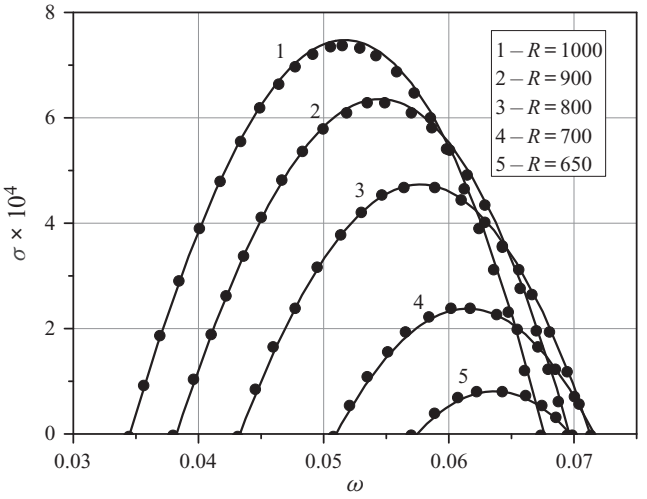

Figure 3. Distributions $\sigma = -\beta_i(\omega)$ of mode S_1 for the compressible Hiemenz flow at $M_e = 1.69$, $T_e^* = 300$ K, $T_w = T_{ad}$ and $x_1 = 0$: lines, asymptotic solution (2.12); symbols, 2-D-PDE solution of Li & Choudhari (2008).

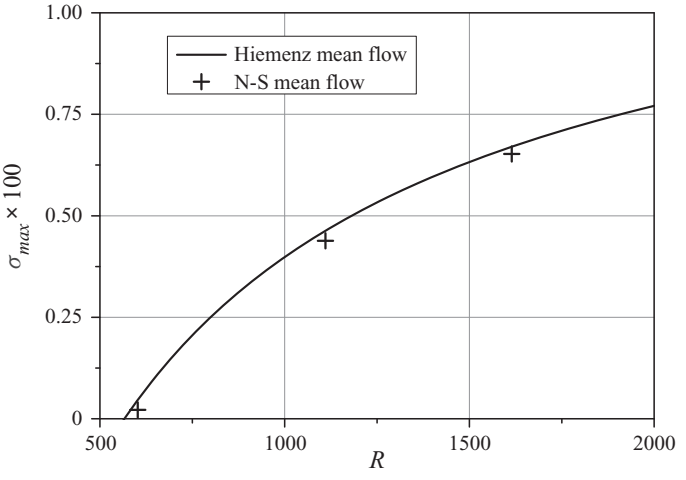

Figure 4. Distribution of maximum growth rate $\sigma_{max}(R)$ for mode S_1 in case C3373a.

mode S_1 as $\alpha \to 0$. This trend is illustrated in figure 5 for a supersonic attachment-line flow at $M_e = 1.55$, $T_e^* = 300$ K, $T_w = T_{ad}$, and in figure 6 for a hypersonic attachment-line flow at $M_e = 5$, $T_e^* = 300$ K, $T_w = 0.7T_e$. In the first case, the most unstable are oblique waves having the wave-front angle $\psi = \tan^{-1}(\alpha/\beta_r) \approx 42^\circ$. In the second case, the most unstable are plane waves of $\alpha = 0$.

This situation is similar to the case of boundary layer flow on a flat plate. For moderate supersonic speeds, the dominant attachment-line instability behaves as the TS-like first mode. It is natural to assume that for sufficiently large M_e, the dominant instability is associated with the Mack second mode of acoustic nature. Indeed, figure 7 shows that there are fast and slow modes of the discrete spectrum. Owing to their synchronisation in the frequency band between the two vertical dashed lines, the slow mode becomes

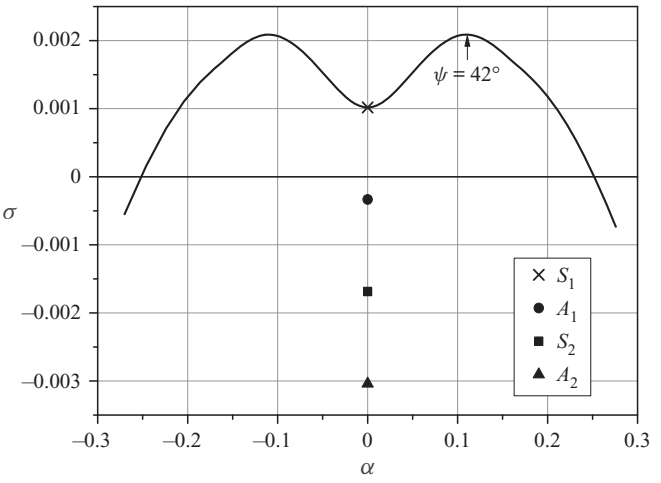

Figure 5. Growth rate $\sigma(\alpha)$ at $R = 1000$, $\omega = 0.0568$ and $x_1 = 0$. The compressible Hiemenz mean flow at $M_e = 1.55$, $T_e^* = 300$ K, $T_w = T_{ad}$: line, 3-D mode (2.16); symbols, quasi-2-D modes (2.12); $\psi = \tan^{-1}(\alpha/\beta_r)$, wave front angle.

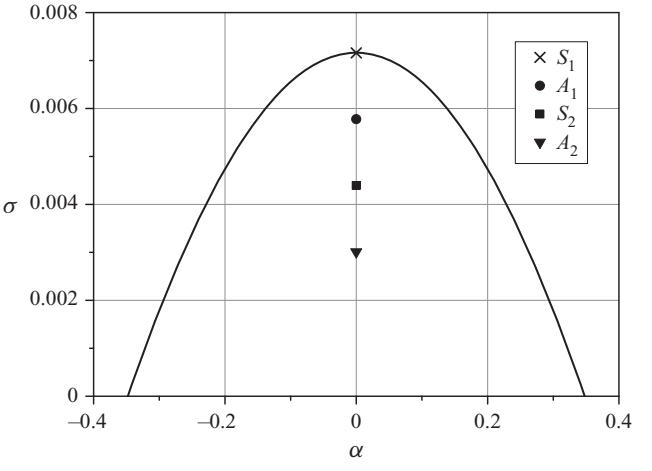

Figure 6. Growth rate $\sigma(\alpha)$ at $R = 1000$, $\omega = 0.5479$ and $x_1 = 0$. The compressible Hiemenz mean flow at $M_e = 5$, $T_e^* = 300$ K, $T_w = 0.7T_e$: line, 3-D mode (2.16); symbols, quasi-2-D modes (2.12).

more unstable while the fast mode becomes more stable. This behaviour is in full accordance with the flat-plate case (see, for example, Fedorov 2011 and Fedorov & Tumin 2011). Therefore, in what follows, we use the terminology of Mack for the dominant attachment-line instabilities. Further analysis is focused on the close vicinity of the attachment line and all computations are performed at $x_1 = 0$.

It should also be noted that the foregoing results contradict the statement of Xi *et al.* (2021) that the attachment-line mode associated with the Mack second mode is absent if the basic flow is calculated with boundary layer assumptions.

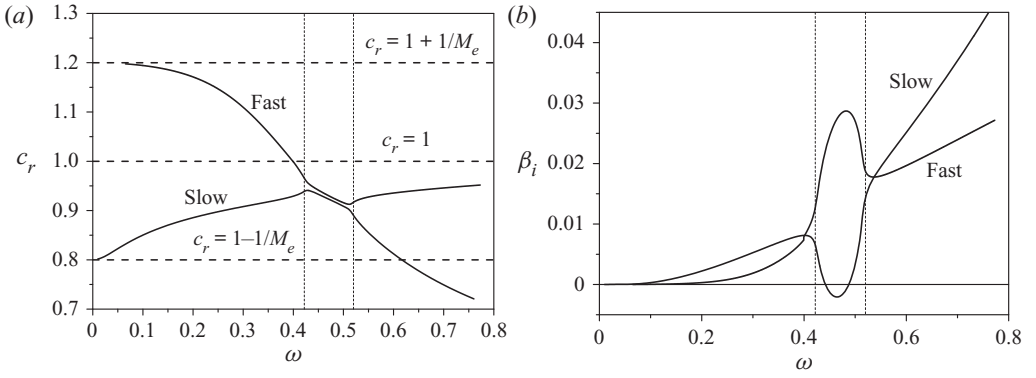

Figure 7. Phase speeds $c_r(\omega) = (\omega/\beta)_r$ and the spatial decrements $\beta_i(\omega)$ of fast and slow modes at $R = 4000$ and $\alpha = 0$ for the compressible Hiemenz mean flow at $M_e = 5$, $T_e^* = 300$ K, $T_w = 5.308T_e \approx T_{ad}$ and $x_1 = 0$: horizontal dashed lines, phase speeds of 2-D fast and slow acoustic waves of zero angle of incidence ($c_r = 1 \pm 1/M_e$) and vortical/entropy waves ($c_r = 1$).

3. Parametric studies

Assume that the laminar–turbulent transition is associated with the spatial growth of unstable waves propagating along the attachment line. If the location of an instability source, $z = z_0$, is known and the initial amplitudes of unstable waves weakly depend on frequency, the transition onset point, z_{tr}, is estimated as (Lin & Malik 1995)

$$N_{tr} = \sigma_{max}(R_{tr})(z_{tr} - z_0), \tag{3.1}$$

where $\sigma_{max}(R) = max_{\omega,\alpha}[-\beta_i(\omega, \alpha, R)]$, and N_{tr} is the empirically determined N-factor. Usually, R_{tr} is plotted as a function of $z_{tr} - z_0$ at a fixed value of N_{tr} (Lin & Malik 1995).

If z_0 is unknown or receptivity is distributed along the attachment line, one can use the following conservative approach. In the vicinity of critical Reynolds number R_{cr} : $\sigma_{max}(R_{cr}) = 0$, the growth rate is approximated as $\sigma_{max}(R) \approx (\mathrm{d}\sigma_{max}/\mathrm{d}R)(R_{cr})(R - R_{cr})$. Substitution of this approximation into (3.1) gives

$$R_{tr} \approx R_{cr}(1 + \delta), \quad \delta = \frac{N_{tr}}{R\dfrac{\mathrm{d}\sigma^*_{max}}{\mathrm{d}R}(R_{cr})L^*_z}, \tag{3.2}$$

where σ^*_{max} is the dimensional growth rate and L^*_z is the leading-edge spanwise scale. In the majority of practical cases, $\delta \ll 1$, and the transition onset Reynolds number is estimated as $R_{tr} = R_{cr}$. This criterion indicates that at $R > R_{tr}$, transition occurs somewhere on a sufficiently long attachment line.

Consider air flow of $\gamma = 1.4$ and $Pr = 0.72$ using the power law for the viscosity coefficient: $\mu(T) = T^m$. With this choice of the temperature–viscosity dependency, the mean-flow profiles (2.1*a–c*) are functions of the two parameters only: the local Mach number M_e and the wall-temperature ratio $T_f = T^*_w/T^*_r$. Therefore, the power law is widely used in parametric studies. Depending on flow temperature, the exponent varies from $m = 1$ for relatively small T to $m = 0.7$ for high temperatures. Hereafter, we use $m = 0.75$. In § 4, it is shown that the critical Reynolds numbers predicted at this value of m are close to those in the case of the Sutherland law. Because the dominant attachment-line instability is captured by the asymptotic solution (2.16), further stability computations are performed using this solution only.

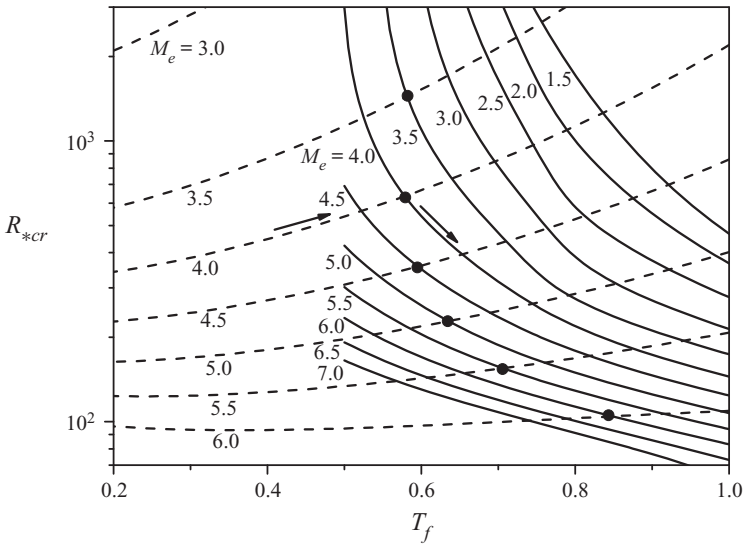

Figure 8. Distributions of the reduced critical Reynolds number $R_{*cr}(T_f)$ at various M_e: dashed lines, quasi-2-D waves of the second mode; solid lines, 3-D waves of the first mode.

Figure 8 shows distributions of the reduced critical Reynolds number $R_{*cr}(T_f)$ at various values of M_e. The solid lines are relevant to 3-D waves of the first mode and the dashed lines refer to 2-D waves of the second mode. As an example, consider the case of $M_e = 4$ marked by arrows. In the region of small T_f, where the second mode is dominant, R_{*cr} monotonically increases with T_f and reaches a value shown by the black circle. Starting from this point, the first mode takes over and R_{*cr} decreases with T_f. The circles form a distribution of maximal R_{*cr}. As T_f decreases, $R_{*cr,max}(T_f)$ quickly increases, and ultimately the attachment-line flow becomes stable for $T_f < 0.58$.

Using the distributions in figure 8, we identify regions in the $M_e - T_f$ space where different instabilities are dominant (figure 9). This diagram allows us to predict what mode could trigger transition under different experimental conditions shown by symbols. For example, in the experiments of Gaillard *et al.* (1999) and Holden & Kolly (1995), the second mode is dominant. In the experiments of Murakami, Stanewsky & Krogmann (1996), some points lie in the stable region, where transition is not relevant to the linearly unstable modes and the bypass scenario is most likely.

4. Comparison with experiments

Consider the transition data obtained on smooth swept-cylinder models tested in different wind tunnels. The local flow parameters are given in tables 1 and 2 of Appendix A. The transition onset Reynolds numbers R_{*tr} are shown by circles in figure 10. The white (black) symbols are related to the cases where the first (second) mode is dominant. The corresponding theoretical predictions, which were performed using the distributions in figure 8 and the criterion $Re_{*tr} = Re_{*cr}$, are shown by the oblique and straight crosses.

At moderate sweep Mach numbers ($M_e < 3.5$), where the first mode is dominant, a large scatter of the theoretical points arises from the high sensitivity of the first-mode growth rates to the wall temperature ratio T_f. For $M_e > 4$, where the second mode is dominant, the scatter is relatively small. In this region, both experimental and theoretical values of R_{*tr} decrease with M_e in a similar way. However, the theoretical points lie

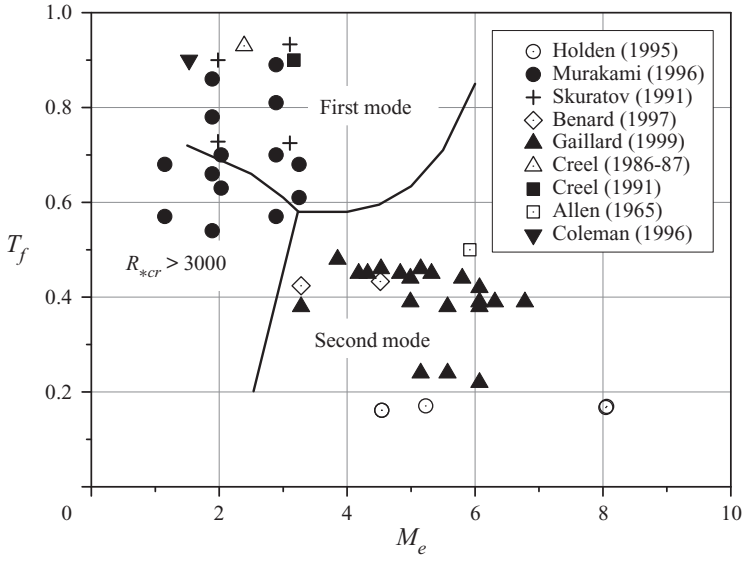

Figure 9. Boundaries in the M_e–T_f space between regions associated with instability of different modes (lines). Symbols show the conditions under which transition is observed in supersonic attachment-line flows on smooth swept cylinders (see tables 1 and 2 of Appendix A).

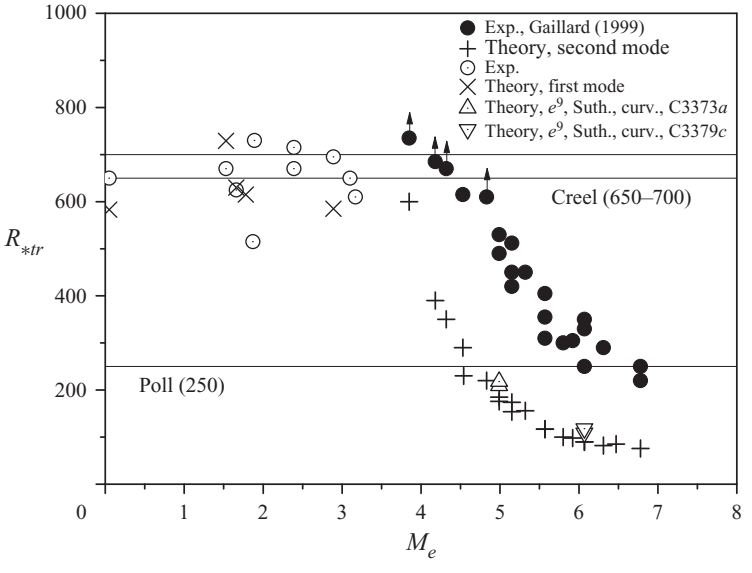

Figure 10. Transition onset Reynolds numbers versus local Mach number. At the arrowed points, transition is not observed on the model.

significantly below the experimental ones. Stability computations using the Sutherland law for the viscosity coefficient and accounting for the leading-edge curvature effect led to a small reduction of this discrepancy (see the white triangles). Similar computations using the mean flow predicted by our N-S solver did not eliminate the discrepancy either.

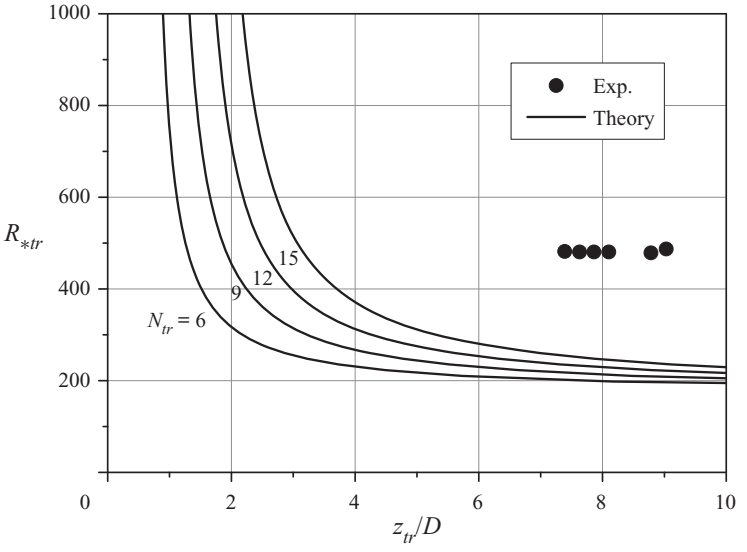

Figure 11. Transition onset Reynolds number versus z_{tr} measured from the upstream side boundary ($z_0 = 0$) of the swept-cylinder model in case C3373a. Cylinder diameter is $D = 33$ mm.

For example, in case C3373a, the relative increase of the critical Reynolds number is $(R_{*cr,\text{N-S}} - R_{*cr,Hiemenz})/R_{*cr,Hiemenz} \approx 2.2\,\%$ only.

Because the second-mode instability has frequency approaching the MHz range (e.g. $f^* \approx 700$ kHz in case C3379c), it is natural to assume that molecular relaxation processes can affect the instability growth. Dealing with air, which is predominantly diatomic gas, one should address the effects associated with rotational and vibrational relaxations. Bertolotti (1998) showed that the vibrational relaxation becomes important when the flow temperature surpasses approximately 800 K. Because the experiments of Gaillard *et al.* (1999) were performed at the total temperature $T_t \approx 700$ K, this effect seems to be small. The rotational relaxation effect can be approximated using the bulk viscosity μ_v. Bertolotti (1998) showed that the ratio $\bar{\mu}_v = \mu_v/\mu$ varies from 0.57 to 1 within the temperature range of 200–1200 K. For first-cut estimates, we choose $\bar{\mu}_v = 0.8$ and calculated the critical Reynolds number R_{*cr} in the case C3379c. It turned out that the relative difference

$$[R_{*cr}(\bar{\mu}_v = 0.8) - R_{*cr}(\bar{\mu}_v = 0)]/R_{*cr}(\bar{\mu}_v = 0) \approx 25\,\%, \tag{4.1}$$

is not sufficient to compensate the discrepancy with Gayllard's data shown in figure 10. Nevertheless, real gas effects on the second-mode instability of attachment-line flow deserve comprehensive studies.

Computations using the less conservative correlation (3.1) demonstrate a similar discrepancy. As shown in figure 11, even at $N_{tr} = 15$, the experimental points are well above the theoretical line. Because the experimental values of R_{*tr} are practically independent of z_{tr}/D, the side boundary effect associated with the limited span of the model seems to be insignificant. At the experimentally observed transition onset $z_{tr}/D \approx 8$, the sensitivity of R_{*tr} to N_{tr} is quite low: $N_{tr}\Delta R_{*tr}/(R_{*tr}\Delta N_{tr}) \approx 0.2$. Therefore, the poor agreement between theory and experiment is not relevant to uncertainty in N_{tr}. Most likely, at high sweep Mach numbers ($M_e > 4$), we encounter an unknown effect that does not fit to the concept of transition owing to linear instability.

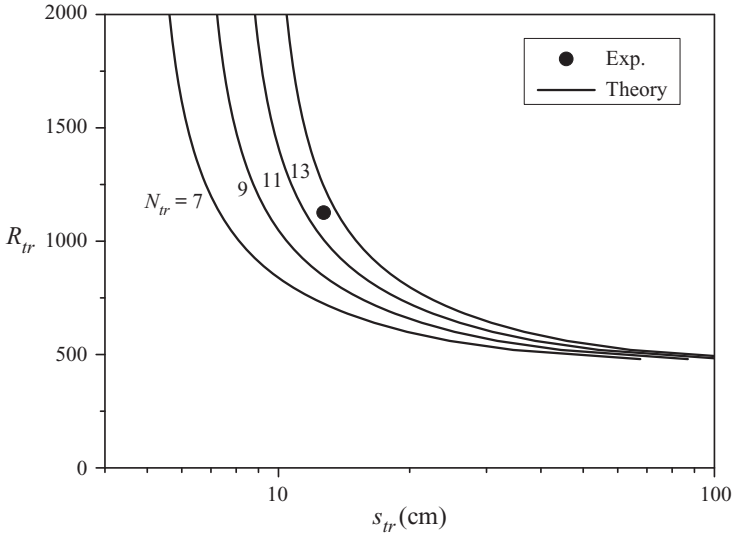

Figure 12. Transition onset Reynolds number versus z_{tr} measured by Creel *et al.* (1986) from the upstream side boundary ($z_0 = 0$) of the swept-cylinder model at $M_\infty = 3.5$ and $\Lambda = 60^\circ$.

Nevertheless, for moderate supersonic cases ($M_e < 4$), the linear stability theory predicts R_{*tr} satisfactorily (the white points in figure 10). In the experiment of Creel, Beckwith & Chen (1986, 1987), $M_\infty = 3.5$, $\Lambda = 60^\circ$ and $T_w^*/T_t^* \approx 0.9$, where the first mode is dominant, the experimental point corresponds to $N_{tr} \approx 12$ that is reasonable for quiet free-stream conditions in the Mach 3.5 pilot low-disturbance wind tunnel (figure 12). Note that in this case, the model is not long enough to reach the infinite swept attachment-line limit: $R_{tr}(z) \to R_{cr}$.

5. Concluding remarks

The theoretical model, which is based on the compressible Hiemenz solution for the mean flow and the successive approximation procedures for small disturbances, has been employed to the linear stability analysis of high-speed attachment-line flows. It was shown that the dominant attachment-line instability is captured by the asymptotic solution (2.16) for 3-D waves. This solution tends to the most unstable quasi-2-D mode S_1 predicted by the solution (2.12). The latter agrees well with the 2-D-PDE stability analysis of Li & Choudhari (2008) at $M_e = 1.69$. In the limit $\alpha \to 0$, the 3-D mode is expressed as a sum of quasi-2-D symmetric S_j and antisymmetric A_j modes ($j = 1, 2, \ldots$).

Qualitative behaviour of the attachment-line instability is similar to the boundary-layer instability on a flat plate. Namely, at moderate supersonic speeds ($M_e < 4$), the most unstable are oblique waves, which are similar to the TS-like first mode. For $M_e > 4$, the most unstable are plane waves, which are similar to the Mack second mode. These results are in a qualitative agreement with those reported by Xi *et al.* (2021). However, we found that the N-S mean flow solutions, used by Xi *et al.* (2021) in stability analyses, are essentially different from the theoretical (compressible Hiemenz) solutions as well as our N-S solutions, while the latter two agree well. Detailed verification of the N-S solver of Xi *et al.* could help to resolve this mismatch.

It was shown that, similar to the Mack second mode, the attachment-line instability is associated with the synchronisation of slow and fast modes of acoustic nature.

This similarity allows us to extrapolate the knowledge gained for Mack modes to the attachment-line instabilities. For example, methods developed for control of the Mack second mode should be applicable to the attachment-line instability at sufficiently large sweep Mach numbers.

The critical Reynolds numbers related to the first and second modes have been calculated in broad ranges of the wall temperature ratio T_f and the local Mach number M_e. Using these dependencies, we identified regions in the T_f–M_e space, where one of these modes is dominant. This allows for quick predictions of what instability could trigger transition under different experimental conditions.

Using the transition onset criterion, $Re_{*tr} = Re_{*cr}$, we have performed point-by-point comparisons of our theoretical predictions with available transition data obtained on smooth swept cylinders in supersonic and hypersonic wind tunnels. In the cases of $M_e < 4$, where the first mode is dominant, the linear stability theory predicts R_{*tr} satisfactorily.

In the cases of $M_e > 4$, where the Mack second mode is dominant, the theory captures a significant decrease of R_{*tr} with M_e reported by Gaillard *et al.* (1999). However, the theoretical points lie well below the experimental ones. Stability computations using the N-S mean flow and accounting for the leading-edge curvature effect did not eliminate this discrepancy. First-cut estimates of real gas effects associated with the vibrational and rotational relaxations of diatomic molecules did not help either. For $M_e > 6$, the experimental values of transition onset Reynolds number approaches the contamination criterion of Poll, $R_* = 250$, and the corresponding theoretical values of Re_{*cr} are essentially below this level.

These results contradict the generally accepted assumption that, for $R_* \leq 250$, the attachment-line flow must be stable. Most likely, we encounter an unknown effect that does not fit to the concept of transition owing to the second-mode instability in the experiments of Gaillard *et al.* (1999) at $M_e > 4$. To resolve the contradiction, it is planned to perform direct numerical simulations of disturbances propagating along the attachment line on a swept cylinder and compare the numerical results with the stability theory and available experimental data.

Funding. The reported study was funded by RFBR, project number 20-08-00296.

Declaration of interests. The authors report no conflict of interest.

Author ORCIDs.
Alexander V. Fedorov http://orcid.org/0000-0003-1623-7240;
Ivan V. Egorov http://orcid.org/0000-0003-1190-9941.

Appendix A. Flow parameters in wind-tunnel experiments

Table 1 (taken from Gaillard *et al.* 1999) shows the flow parameters and the reduced Reynolds number R_{*tr} at the transition onset on smooth swept cylinders tested in different wind tunnels. Table 2 shows the same parameters for the experiments of Gaillard *et al.* (1999) carried out in a low-enthalpy hypersonic blowdown wind tunnel. Each case is identified by a four-digit number: the first two digits give the cylinder diameter in millimetres and the last two digits, the sweep angle in degrees. In these tables, M_∞ is free-stream Mach number, T_w/T_t is the ratio of wall temperature to stagnation temperature, and $R_{D\infty,tr}$ is the transition onset Reynolds number based on the free-stream parameters and the cylinder diameter.

Case	M_∞	Λ°	T_w/T_t	M_e	$Re_{D\infty,tr} \times 10^{-5}$	R_{*tr}
Whitehead & Dunavant (1965)	6.8	80	0.5	5.92	>4.2	>305
Creel *et al.* (1986, 1987)	3.5	45	0.9	1.66	7	625
	3.5	60	0.9	2.39	8	715
	3.5	60	0.9	2.39	7	670
Creel (1991)	3.5	76	0.9	3.17	6.55	610
Skuratov & Fedorov (1991)	6	45	0.8	1.87	7	515
	6	60	0.8	3.1	9.2	650
Holden & Kolly (1995)	10.6	60	0.28	3.57	5.7–7.75	406–471
	10.5	66.5	0.26	4.54	7.4–9.7	464–542
	10.6	75	0.26	6.47	<7.3	<383
	10.6	80	0.26	8.06	<10.15	<374
Murakami *et al.* (1996)	5	45	0.75	1.89	12	730
	5	60	0.75	2.89	9	695
Coleman *et al.* (1996)	1.6	76	0.9	1.53		>670

Table 1. Flow parameters on smooth models.

Case	M_∞	Λ°	T_w/T_t	M_e	$Re_{D\infty,tr} \times 10^{-5}$	R_{*tr}
C1480	8.15	80	0.39	6.78	2.74	220
C1980	8.15	80	0.39	6.78	3.53	250
C3381	7.14	81	0.39	6.31	3.9	290
C3379a	7.14	79.5	0.39	6.07	4.6	330
C3379b	7.14	79.5	0.42	6.07	5.7	350
C3379c	7.14	79.5	0.38	6.07	3.7	300
C1978	7.14	78	0.44	5.8	3.63	300
C3376a	7.14	76.5	0.38	5.57	5.6	405
C3376b	7.14	76.5	0.38	5.57	4.3	355
C3375	7.14	75	0.45	5.32	6.8	450
C3374a	7.14	74	0.46	5.15	8.55	512
C3374b	7.14	74	0.38	5.15	5.22	420
C3373a	7.14	73	0.39	4.99	6.8	490
C3373b	7.14	73	0.44	4.99	8.5	530
C3372	7.14	72	0.45	4.83	>11	>610
C3370	7.14	70	0.46	4.53	10.4	615
C3369	7.14	68.5	0.45	4.32	>11.6	>670
C3368	7.14	67.5	0.45	4.18	>12	>685
C3365	7.14	65	0.48	3.85	>13.8	>735
C3379C	7.14	79.5	0.22	6.07	<2.48	<250
C3376C	7.14	79.5	0.24	5.57	3.15	310
C3374C	7.14	74	0.24	5.15	5.75	450

Table 2. Flow parameters on smooth models of Gaillard *et al.* (1999), $T_\infty \approx 70$ K.

Appendix B. Verification of the mean-flow solutions

Verification of the N-S mean-flow solvers is performed for the case, which is identified by Xi *et al.* (2021) as C3376a,

$$M_\infty = 7.14, \quad \Lambda = 76.5^\circ, \quad T^*_\infty = 69.84, \quad T^*_w/T^*_\infty = 3.95, \quad Re_{r,\infty} = 5.9755 \times 10^5, \tag{B1a–e}$$

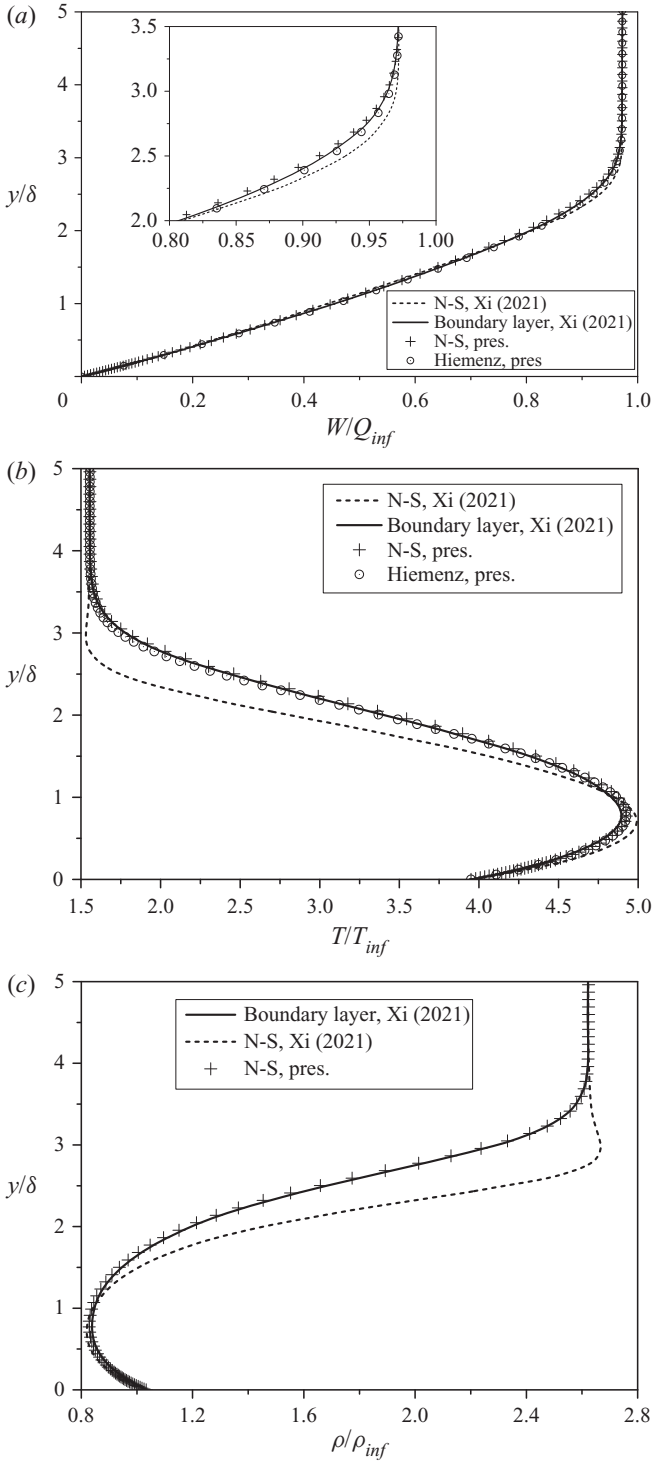

Figure 13. Comparison of the mean-flow profiles in case (B1). Profiles shown by the solid and dashed lines were scanned from figure 29 of Xi *et al.* (2021).

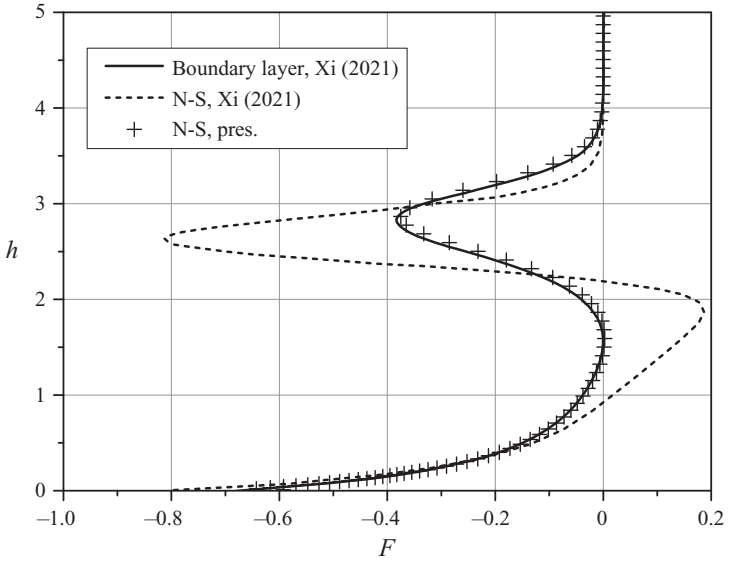

Figure 14. The profiles of $F(h)$ along the wall-normal distance $h = y/\delta$ scanned from figure 6 of Xi *et al.* (2021): solid line, compressible Hiemenz solution; dashed line, N-S solution; black crosses, our N-S solution.

the length scale is $\delta = 1.4937 \times 10^{-4}$ m and the cylinder radius is $r^* = 33$ mm. Note that $Re_{r,\infty}$ differs from the case C3376a of Gaillard *et al.* (1999) where the diameter (not radius) of the cylinder is 33 mm and the correct Reynolds number is $Re_{r,\infty} = 2.8 \times 10^5$ that is half of the experimental value.

The upper edge parameters predicted by the inviscid flow theory of Rechotko & Beckwith (1958) are in perfect agreement with those resulted from our N-S solution:

$$\left.\begin{aligned} (W_e^*/Q_\infty^*)_{theory} = 0.97237, \quad (W_e^*/Q_\infty^*)_{\text{N-S}} = 0.97237 \\ (T_e^*/T_\infty^*)_{theory} = 1.5556, \quad (T_e^*/T_\infty^*)_{\text{N-S}} = 1.5555 \end{aligned}\right\}. \tag{B2}$$

Figure 13 shows (*a*) the mean-flow profiles resulting from the compressible Hiemenz solution (our computations) agree well with the boundary-layer approximation reported by Xi *et al.* (2021); (*b*) the mean-flow profiles predicted by our N-S solver agree well with the theoretical profiles of item a); (*c*) the N-S mean-flow profiles calculated by Xi *et al.* (2021) disagree with both the theoretical profiles of item a) and the profiles predicted by our N-S solver.

Inviscid instability is associated with the generalised inflection points at which

$$F(h) \equiv \partial/\partial h(\rho(\partial W/\partial h)) = 0, \quad h = y/\delta. \tag{B3}$$

Figure 14 compares the function $F(h)$ scanned from figure 6 of Xi *et al.* (2021) with that predicted by our N-S solver. The latter (black crosses) agrees well with $F(h)$ of the compressible Hiemenz solution (the solid line), while $F(h)$ resulting from the N-S solution of Xi *et al.* (2021) (the dashed line) is essentially different. Because the N-S solution of Xi *et al.* (2021) has incorrect generalised inflection points, its stability characteristics are most likely erroneous.

References

Balakumar, P. & Trivedi, P.A. 1998 Finite amplitude stability of attachment line boundary layers. *Phys. Fluids* **10**, 2228–2237.

Benard, E., Gaillard, L. & Alziary de Roquefort, T. 1997 Influence of roughness on attachment line boundary layer transition in hypersonic flow. *Exp. Fluids* **22**, 286–291. Springer-Verlag.

Benard, E., Sidorenko, A. & Raghunathan, S. 2002 Transitional and turbulent heat transfer of swept cylinder attachment line in hypersonic flow. In *40th AIAA Aerospace Sciences Meeting and Exhibit*. *AIAA Paper 2002*-0551. AIAA.

Bertolotti, F.P. 1998 The influence of rotational and vibrational energy relaxation on boundary-layer stability. *J. Fluid Mech.* **372**, 93–118.

Bouthier, M. 1972 Stabilite lineaire des ecoulements presque paralleles. Part I. *J. Mec.* **11**, 599–621.

Bouthier, M. 1973 Stabilite lineaire des ecoulements presque paralleles. Part II. La couche limite de Blasius. *J. Mec.* **12**, 75–95.

Coleman, C.P., Poll, D.I.A., Laub, J.A. & Wolf, S.W.D. 1996 Leading edge transition on a 76 degree swept cylinder at Mach number 1.6. In *Fluid Dynamics Conference 17 June 1996 – 20 June 1996. AIAA Paper 96*-2082. AIAA.

Creel, T.R. 1991 Effect of sweep angle and passive relaminarization devices on a supersonic swept-circular boundary layer. In *29th Aerospace Sciences Meeting*. *AIAA Paper 91*-0066. AIAA.

Creel, T.R., Beckwith, I.E. & Chen, F.J. 1986 Effects of wind-tunnel noise on swept-cylinder transition at Mach 3.5. In *Fluid Dynamics and Co-located Conferences*. *AIAA Paper 86*-1085. AIAA.

Creel, T.R., Beckwith, I.E. & Chen, F.J. 1987 Transition on swept leading edges at Mach 3.5. *J. Aircraft* **24** (10), 710–717.

Egorov, I.V. 1992 Influence of real gas properties on the integral aerodynamic coefficients. *Fluid Dyn.* **27** (4), 573–579.

Fedorov, A. 2011 Transition and stability of high-speed boundary layers. *Annu. Rev. Fluid Mech.* **43** (1), 79–95.

Fedorov, A. & Tumin, A. 2011 High-speed boundary-layer instability: old terminology and a new framework. *AIAA J.* **49** (8), 1647–1657.

Gaillard, L., Benard, E. & Alziary de Roquefort, T. 1999 Smooth leading edge transition in hypersonic flow. *Exp. Fluids* **26** (1), 169–176.

Gaster, M. 1967 On the flow along swept leading edges. *Aeronaut. Q.* **18** (Part 2), 165–184.

Gaster, M. 1974 On the effects of boundary-layer growth on flow stability. *J. Fluid Mech.* **66**, 465–480.

Gennaro, E.M., Rodríguez, D., Medeiros, M.A.F. & Theofilis, V. 2013 Sparse techniques in global flow instability with application to compressible leading-edge flow. *AIAA J.* **51** (9), 2295–2303.

Hall, P. & Malik, M.R. 1986 On the instability of a three-dimensional attachment line boundary layer: weakly nonlinear theory and a numerical simulation. *J. Fluid Mech.* **163**, 257–282.

Hall, P., Malik, M. & Poll, D. 1984 On the stability of an infinite swept attachment-line boundary layer. *Proc. R. Soc. Lond.* A **395**, 229–245.

Holden, M.S. & Kolly, J.M. 1995 Attachment line transition studies on swept cylindrical leading edges at Mach numbers from 10 to 12. In *Fluid Dynamics Conference 19 June 1995 – 22 June* 1995. *AIAA Paper 95*-2279. AIAA.

Li, F. & Choudhari, M.M. 2008 Spatially developing secondary instabilities and attachment line instability in supersonic boundary layers. In *46th AIAA Aerospace Sciences Meeting and Exhibit*. *AIAA paper 2008-590*. AIAA.

Lin, R.-S. & Malik, M.R. 1995 Stability and transition in compressible attachment-line boundary-layer flow. *SAE Technical Paper* 952041.

Lin, R.-S. & Malik, M.R. 1996 On the stability of attachment-line boundary layers. Part 1. The incompressible swept Hiemenz flow. *J. Fluid Mech.* **311**, 239–255.

Mack, L.M. 1975 Linear stability theory and the problem of supersonic boundary-layer transition. *AIAA J.* **13** (3), 278–289.

Mack, L.M. 1979 On the stability of the boundary layer on a transonic swept wing. In *17th Aerospace Sciences Meeting. AIAA Paper 79*-0264. AIAA.

Morkovin, M.V., Reshotko, E. & Herbert, T. 1994 Transition in open flow systems – a reassessment. *Bull. Am. Phys. Soc.* **39** (9), 1–31.

Murakami, A., Stanewsky, E. & Krogmann, P. 1996 Boundary-layer transition on swept cylinders at hypersonic speeds. *AIAA J.* **34** (4), 649–654.

Nayfeh, A.H. 1980 Stability of three-dimensional boundary layers. *AIAA J.* **18** (4), 406–416.

Pfenninger, W. 1965 Flow phenomena at the leading edge of swept wings. In *Recent Developments in Boundary Layer Research: AGARDograph 97*, Part 4.

POLL, D.I.A. 1979 Transition in the infinite swept attachment line boundary layer. *Aeronaut. Q.* **30** (4), 607–629.

POLL, D.I.A. 1994 Implication of 3-D transition mechanisms on the performance of space vehicles. In *Second European Symposium for Space Vehicles ESA*. ISBN 92-9092-310-5, pp. 175–182.

RECHOTKO, E. & BECKWITH, I.E. 1958 Compressible laminar boundary layer over a yawed infinite cylinder with heat transfer and arbitrary Prandtl number. *NACA Tech. Rep.* 1379.

SEMISYNOV, A.I., FEDOROV, A.V., NOVIKOV, V.E., SEMIONOV, N.V. & KOSINOV, A.D. 2003 Stability and transition on a swept cylinder in a supersonic flow. *J. Appl. Mech. Tech. Phys.* **44** (2), 212–220.

SKURATOV, A.S. & FEDOROV, A.V. 1991 Supersonic boundary layer transition induced by roughness on the attachment line of a yawed cylinder. *Fluid Dyn.* **26**, 816–822.

SPALART, P.R. 1988 Direct numerical study of leading edge contamination. *AGARD CP* 438.

THEOFILIS, V., FEDOROV, A.V. & COLLIS, S.S. 2006 Leading-edge boundary layer flow (Prandtl's vision, current developments and future perspectives). In *IUTAM Symposium on One Hundred Years of Boundary Layer Research. Solid Mechanics and Its Applications* (ed. G.E.A. Meier, K.R. Sreenivasan & H.J. Heinemann), vol. 129, pp. 73–82. Springer.

THEOFILIS, V., FEDOROV, A., OBRIST, D. & DALLMAN, U.W.E.C. 2003 The extended Görtler–Hämmerlin model for linear instability of three-dimensional incompressible swept attachment-line boundary layer flow. *J. Fluid Mech.* **487**, 271–313.

TUMIN, A. 2006 Biorthogonal eigenfunction system in the triple-deck limit. *Stud. Appl. Maths* **117** (2), 165–190.

TUMIN, A.M. 2007 Three-dimensional spatial normal modes in compressible boundary layers. *J. Fluid Mech.* **586**, 295–322.

TUMIN, A. 2011 The biorthogonal eigenfunction system of linear stability equations: a survey of applications to receptivity problems and to analysis of experimental and computational results. In *41st AIAA Fluid Dynamics Conference and Exhibit*. *AIAA Paper 2011*-3244. AIAA.

WHITEHEAD, A.H. JR. & DUNAVANT, J.C. 1965 A study of pressure and heat transfer over an 80° sweep slab delta wing in hypersonic flow. *NASA TN D*-2708.

XI, Y., REN, J. & FU, S. 2021 Hypersonic attachment-line instabilities with large sweep Mach numbers. *J. Fluid Mech.* **915**, A44.